



## A cell-based smoothed radial point interpolation method (CS-RPIM) for static and free vibration of solids

X.Y. Cui<sup>a,b</sup>, G.R. Liu<sup>b,c</sup>, G.Y. Li<sup>a,\*</sup>

<sup>a</sup> State Key Laboratory of Advanced Design and Manufacturing for Vehicle Body, Hunan University, Changsha 410082, PR China

<sup>b</sup> Centre for Advanced Computations in Engineering Science (ACES), Department of Mechanical Engineering, National University of Singapore, 9 Engineering Drive 1, Singapore 117576, Singapore

<sup>c</sup> Singapore-MIT Alliance (SMA), E4-04-10, 4 Engineering Drive 3, Singapore 117576, Singapore

### ARTICLE INFO

#### Article history:

Received 13 February 2009

Accepted 30 July 2009

Available online 22 August 2009

#### Keywords:

Numerical method

Meshfree method

Radial point interpolation method (RPIM)

Gradient smoothing operation

Subdomain stabilized conforming integration

### ABSTRACT

A cell-based smoothed radial point interpolation method (CS-RPIM) based on the generalized gradient smoothing operation is proposed for static and free vibration analysis of solids. In present method, the problem domain is first discretized using triangular background cells, and each cell is further divided into several smoothing cells. The displacement field function is approximated using RPIM shape functions which have Kronecker delta function property. Supporting node selection for shape function construction uses the efficient T2L-scheme associated with edges of the background cells. The system equations are derived using the generalized smoothed Galerkin (GS-Galerkin) weak form, and the essential boundary conditions are imposed directly as in the finite element method (FEM). The effects of the number of divisions smoothing cells on the solution properties of the CS-RPIM are investigated in detail, and preferable numbers of smoothing cells is recommended. To verify the accuracy and stability of the present formulation, a number of numerical examples are studied to demonstrate numerically the efficiency of the present CS-RPIM.

© 2009 Elsevier Ltd. All rights reserved.

### 1. Introduction

In the past decades, various meshfree methods including smooth particle hydrodynamics [1], diffuse element method (DEM) [2], element free Galerkin (EFG) method [3], reproducing kernel particle method (RKPM) [4], finite point method (FPM) [5], H-P clouds [6], meshless local Petrov–Galerkin (MLPG) method [7], point interpolation method (PIM) [8], radial point interpolation method (RPIM) [9], etc., have been proposed and applied in more and more fields of particular engineering and scientific problems [10]. In any numerical method creating shape functions is an essential issue, and currently there are basically two major types of methods: moving least squares (MLS) and point interpolation method (PIM). The RPIM shape functions created using local irregular nodes are preferred in many ways, because (1) they have the Kronecker delta function property, which allows straightforward imposition of essential boundary conditions and (2) very irregularly distributed nodes can be used.

In the weak form meshfree methods, background cells are commonly used to implement the Gaussian integration to evaluate the stiffness matrix. Due to the complexity involved using the Gauss integration, the nodal integration techniques have

been developed by performing integrals based on the nodes [11]. Beissel and Belytschko [11] demonstrated that the nodal integration of EFG resulted in a spatial instability due to the under integration of the weak form. They proposed a stabilized procedure to eliminate the spatial instability. Bonet and Kulasegaram [12] presented a least-square stabilization technique to eliminate spurious mode in nodal integration. Chen et al. [13] proposed a stabilized conforming nodal integration using a strain smoothing technique, and this method can eradicate spatial instability in nodal integration and reproduce a linear field exactly. Based on the strain smoothing technique [13], a generalized gradient smoothing technique has been suggested [14] to accommodate discontinuous functions. The generalized gradient smoothing technique forms the theoretical foundation for the linearly conforming radial point interpolation method (LC-RPIM or NS-RPIM) where discontinuous RPIM shape functions are used [15]. It has been found that NS-RPIM can provide upper bound solution in energy norm for models of not too coarse mesh for force-driving problems. Although the NS-RPIM has been proven spatially stable and convergent, it is not temporally stable, which leads to the development of the edge-based smoothed radial point interpolation method (ES-RPIM) [16]. It has been found that one of the most significant features of all the methods using RPIM shape functions is that it works ideally well for extremely irregularly distributed nodes: the nodes can be virtually random. The moment matrix will never be singular, as long as some basic

\* Corresponding author. Tel.: +86 731 8821717; fax: +86 731 8822051.  
E-mail address: gyli@hnu.cn (G.Y. Li).

rules are followed [10]. In addition, the RPIM shape functions have, in theory, unlimited order of local consistence and hence ideal for creating functions in G spaces [10]. These unique features give the RPIM shape functions a special position in meshfree methods. There are, however, rooms for further improvements on both the solution accuracy and efficiency.

Incorporating meshfree techniques with the standard FEM, Liu et al. [17] proposed a smoothed finite element method (SFEM) by using the strain smoothing technique in FEM settings. The SFEM further divides the elements into some smoothing cells, computes the integrals along the edge of the smoothing cells, and has been proven to have good properties. A more general setting based on the cell-based smoothing idea and the polynomial PIM shape functions is the cell-based smoothed PIM (or CS-PIM) [18]. Due to the use of polynomial PIM shape functions, a carefully formulated coordinate transformation is needed to avoid the singularity in the moment matrix. Clearly in avoiding the singularity of the moment matrix, the use of RPIM shape function is natural and much more straightforward. In the CS-PIM and CS-RPIM, however, only one smoothing cell per triangular background cell is used, and hence the model can be on the soft side, leading to less accurate solutions for some problems with weak constraints.

In the present work, we further improve the CS-RPIM aiming to increase the stiffness of the model by using the SFEM idea of dividing the background cells further into some smoothing cells. In the present CS-RPIM, the problem domain is first discretized using triangular background cells. The support nodes of each node for the local RPIM approximation are selected based on the background cells. The background triangular cells are further divided into several smoothing cells, and the “smoothed” strains in each smoothing cell are obtained using the generalized gradient smoothing technique [19] which allows the use of discontinuous nodal shape functions like the RPIM. The use of the generalized gradient smoothing technique requires only numerical integrations along the edges of the background cells, and the continuity of the assumed displacement field using RPIM can be ensured along the edges of the smoothing cells. The strains in the smoothing cells are assumed to be constants that equal to the “smoothed” strains obtained using the generalized gradient smoothing technique. Therefore there is no need for any numerical integration in computing the stiffness matrix, because the energy is simply a summation of that over all the smoothing cells. To examine the performance of the proposed method, a series of benchmark examples is presented, and excellent results are obtained demonstrating the efficiency and accuracy of the present CS-RPIM method.

## 2. Radial point interpolation method

This section summarizes the RPIM approximation for the field variables using local nodes and the radial basis functions (RBF) augmented with polynomial basis functions [10]. Consider a domain with a set of arbitrarily scattered points  $\mathbf{x}_i$ , ( $i = 1, 2, \dots, n$ ),  $n$  is the number of nodes in the local support domain. The approximation of a function  $u(\mathbf{x})$  in support domain can be expressed in the form of

$$u(\mathbf{x}) = \sum_{i=1}^n R_i(\mathbf{x})a_i + \sum_{j=1}^m P_j(\mathbf{x})b_j = \mathbf{R}^T(\mathbf{x})\mathbf{a} + \mathbf{P}^T(\mathbf{x})\mathbf{b} \quad (1)$$

where  $R_i(\mathbf{x})$  is radial basis function,  $a_i$  the unknown coefficient for functions  $R_i(\mathbf{x})$ ,  $b_j$  the coefficient for polynomial basis  $P_j(\mathbf{x})$ ,  $n$  the number of field nodes in the local support domain and  $m$  determined according to the polynomial basis selected. When  $m = 0$ , pure RBFs are used. Otherwise, the RBF is augmented with  $m$  terms of polynomial basis functions. In the present work, the multi-quadrics RBF (MQ-RBF) [19] is used, which has the following form:

$$R_i(\mathbf{x}) = [(x - x_i)^2 + (y - y_i)^2 + (\alpha_c d_c)^2]^q \quad (2)$$

where  $q$  and  $\alpha_c$  are two shape parameters, which are real and arbitrary and have been examined in detail by Liu [10],  $d_c$  is the equivalent length of the background cell.

The polynomial basis function for two-dimensional domains has the following form:

$$\mathbf{P}^T(\mathbf{x}) = [1, x, y, \dots] \quad (3)$$

The coefficients in Eq. (1) can be determined by enforcing the field function to be satisfied at the  $n$  nodes within the local support domain of the point of interest  $\mathbf{x}$ . This leads to  $n$  linear equations, which can be expressed in the matrix form as

$$\mathbf{U}_s = \mathbf{R}_q \mathbf{a} + \mathbf{P}_m \mathbf{b} \quad (4)$$

where  $\mathbf{U}_s$  is the vector of function values

$$\mathbf{U}_s = \{u_1, u_2, \dots, u_n\}^T \quad (5)$$

$\mathbf{R}_q$  is the moment matrix of RBFs given by

$$\mathbf{R}_q = \begin{bmatrix} R_1(\mathbf{x}_1) & R_2(\mathbf{x}_1) & \dots & R_n(\mathbf{x}_1) \\ R_1(\mathbf{x}_2) & R_2(\mathbf{x}_2) & \dots & R_n(\mathbf{x}_2) \\ \dots & \dots & \dots & \dots \\ R_1(\mathbf{x}_n) & R_2(\mathbf{x}_n) & \dots & R_n(\mathbf{x}_n) \end{bmatrix}_{n \times n} \quad (6)$$

and matrix  $\mathbf{P}_m$  is defined as

$$\mathbf{P}_m = \begin{bmatrix} p_1(\mathbf{x}_1) & p_2(\mathbf{x}_1) & \dots & p_m(\mathbf{x}_1) \\ p_1(\mathbf{x}_2) & p_2(\mathbf{x}_2) & \dots & p_m(\mathbf{x}_2) \\ \vdots & \vdots & \vdots & \vdots \\ p_1(\mathbf{x}_n) & p_2(\mathbf{x}_n) & \dots & p_m(\mathbf{x}_n) \end{bmatrix} \quad (7)$$

As there are  $n+m$  variables in Eq. (4), the additional  $m$  equations should be added by using the following constraint conditions [20]:

$$\sum_{i=1}^n p_j(\mathbf{x}_k) a_i = 0, \quad j = 1, 2, \dots, m \quad (8)$$

Combining Eqs. (4) and (8) yields the following set of equations in the matrix form

$$\tilde{\mathbf{U}}_s = \begin{Bmatrix} \mathbf{U}_s \\ \mathbf{0} \end{Bmatrix} = \begin{bmatrix} \mathbf{R}_q & \mathbf{P}_m \\ \mathbf{P}_m^T & \mathbf{0} \end{bmatrix} \begin{Bmatrix} \mathbf{a} \\ \mathbf{b} \end{Bmatrix} = \mathbf{G} \begin{Bmatrix} \mathbf{a} \\ \mathbf{b} \end{Bmatrix} \quad (9)$$

Solving Eq. (9) yields

$$\begin{Bmatrix} \mathbf{a} \\ \mathbf{b} \end{Bmatrix} = \mathbf{G}^{-1} \begin{Bmatrix} \mathbf{U}_s \\ \mathbf{0} \end{Bmatrix} \quad (10)$$

The approximation of function  $u(\mathbf{x})$  is finally expressed as

$$u(\mathbf{x}) = [\mathbf{R}_q^T(\mathbf{x}) \mathbf{P}_m^T(\mathbf{x})] \mathbf{G}^{-1} \begin{Bmatrix} \mathbf{U}_s \\ \mathbf{0} \end{Bmatrix} = \boldsymbol{\phi}(\mathbf{x}) \mathbf{U}_s \quad (11)$$

In Eq. (11),  $\boldsymbol{\phi}(\mathbf{x})$  is RPIM shape functions corresponding to the nodal value and given by

$$\boldsymbol{\phi}(\mathbf{x}) = [\varphi_1(\mathbf{x}) \quad \varphi_2(\mathbf{x}) \quad \dots \quad \varphi_n(\mathbf{x})] \quad (12)$$

in which

$$\varphi_k(\mathbf{x}) = \sum_{i=1}^n R_i(\mathbf{x}) \bar{G}_{(i,k)} + \sum_{j=1}^m P_j(\mathbf{x}) \bar{G}_{(n+j,k)} \quad (13)$$

where  $\bar{G}_{(i,k)}$  is the element of matrix  $\mathbf{G}^{-1}$ . An approximation function  $u(\mathbf{x})$  can be expressed as

$$u(\mathbf{x}) = \sum_{i=1}^n \varphi_i(\mathbf{x}) u_i \quad (14)$$

The present shape functions possess the reproducing properties due to the addition of polynomial basis, also satisfy the Delta function properties and partition of unity, and always exist because of the adoption of RBFs.

### 3. Brief of basic equations

A solid mechanics problem of static elasticity can be described by equilibrium equation in the domain  $\Omega$  which can be given by

$$\mathbf{L}^T \boldsymbol{\sigma} + \mathbf{b} = \mathbf{0} \quad (15)$$

where  $\mathbf{L}$  is differential operator matrix defined as

$$\mathbf{L} = \begin{bmatrix} \frac{\partial}{\partial x} & 0 \\ 0 & \frac{\partial}{\partial y} \\ \frac{\partial}{\partial y} & \frac{\partial}{\partial x} \end{bmatrix} \quad (16)$$

$\boldsymbol{\sigma}^T = \{\sigma_{xx}, \sigma_{yy}, \sigma_{xy}\}$  is the stress vector and  $\mathbf{b}^T = \{b_x, b_y\}$  is the body force vector.

The stresses relate the strain via the constitutive equation as follows:

$$\boldsymbol{\sigma} = \mathbf{D}\boldsymbol{\varepsilon} \quad (17)$$

in which  $\mathbf{D}$  is the matrix of material constants that defined as follows:

$$\mathbf{D} = \frac{E}{1-\nu^2} \begin{bmatrix} 1 & \nu & 0 \\ \nu & 1 & 0 \\ 0 & 0 & \frac{1-\nu}{2} \end{bmatrix} \text{Plane stress} \quad (18)$$

$$\mathbf{D} = \frac{E(1-\nu)}{(1-\nu)(1-2\nu)} \begin{bmatrix} 1 & \frac{\nu}{1-\nu} & 0 \\ \frac{\nu}{1-\nu} & 1 & 0 \\ 0 & 0 & \frac{1-2\nu}{2(1-\nu)} \end{bmatrix} \text{Plane strain}$$

where  $E$  is Young's modulus and  $\nu$  is Poisson's ratio.

In Eq. (17),  $\boldsymbol{\varepsilon}^T = \{\varepsilon_{xx}, \varepsilon_{yy}, 2\varepsilon_{xy}\}$  is the vector of strains that relates to the displacements by the following compatibility equation:

$$\boldsymbol{\varepsilon} = \mathbf{L}\mathbf{u} \quad (19)$$

where  $\mathbf{u} = \{u_x, u_y\}^T$  is the displacement vector.

Boundary conditions are given as follows:

$$\mathbf{u} = \mathbf{u}_f \text{ on } \Gamma_u \quad (20)$$

$$\mathbf{n}^T \boldsymbol{\sigma} = \mathbf{t}_f \text{ on } \Gamma_t \quad (21)$$

where  $\mathbf{u}_f$  is the specified displacement on the essential boundary  $\Gamma_u$ ,  $\mathbf{t}_f$  is the given traction on the natural boundary  $\Gamma_t$ , and  $\mathbf{n}$  is the unit outward normal matrix expressed as

$$\mathbf{n} = \begin{bmatrix} n_x & 0 \\ 0 & n_y \\ n_y & n_x \end{bmatrix} \quad (22)$$

### 4. Generalized smoothed strain

In the present work, the problem domain is first discretized with three-node triangular cells, which can always be generated efficiently and automatically without much manual operation. Such a background triangular cell is termed as "parent" cell for convenience in our discussion. The edge of a parent cell is called "cell edge". Each "parent" cell is further divided into some non-overlapping smoothing cells  $\Omega_k = \cup_{C=1}^{SC} \Omega_{k(C)}$ , as shown in Fig. 1. The edge of the smoothing cell is called "segment". All the segments of the smoothing cell form the boundary of the smoothing cell, and the boundary is denoted as  $\Gamma_{k(C)}$ . The strain

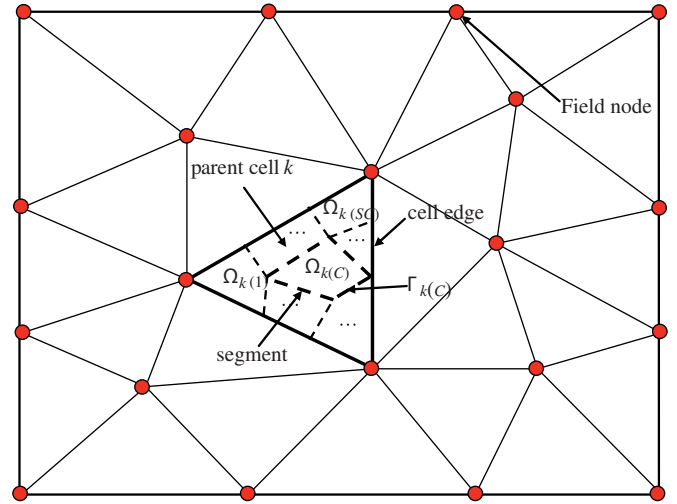


Fig. 1. The problem domain is divided into triangular background cells. Each triangular cell is called parent cell. The  $k$ th parent cell is further divided into SC smoothing cells.

field in the  $C$ th smoothing cell  $\Omega_{k(C)}$  in  $\Omega_k$  is assumed constant that is approximated using following generalized gradient smoothing technique [14]:

$$\bar{\boldsymbol{\varepsilon}}_{k(C)} \equiv \frac{1}{A_{k(C)}} \int_{\Gamma_{k(C)}} \mathbf{n} \cdot \mathbf{u}(\mathbf{x}) d\Gamma \quad (23)$$

where  $\mathbf{u}$  is the assumed displacements using RPIM shape functions that can be discontinuous in the smoothing cell  $\Omega_{k(C)}$ ,  $A_{k(C)}$  the area of the  $C$ th smoothing cell, and  $\mathbf{n}$  the outward normal matrix containing the components of the outward normal vector on the boundary  $\Gamma_{k(C)}$ . Note when the assumed displacement is continuous,  $\bar{\boldsymbol{\varepsilon}}_{k(C)}$  is the so-called smoothed strain: strain obtained from the compatible strain field via smoothing operation. However, when the assumed displacement is discontinuous,  $\bar{\boldsymbol{\varepsilon}}_{k(C)}$  does not exist, and thus rigorously speaking it cannot be called smoothed strain, although we often termed it as "smoothed" strain. A better name for  $\bar{\boldsymbol{\varepsilon}}_{k(C)}$  might be *constructed strain* via boundary flux approximation [10].

Substituting Eq. (14) into Eq. (23), the smoothed strain can also be written in matrix form of

$$\bar{\boldsymbol{\varepsilon}}_{k(C)} = \frac{1}{A_{k(C)}} \sum_{i=1}^{NP} \left( \int_{\Gamma_{k(C)}} \mathbf{n} \cdot \boldsymbol{\phi}_i(\mathbf{x}) d\Gamma \right) \mathbf{u}_i = \sum_{i=1}^{NP} \bar{\mathbf{B}}_{k(C)}^i \mathbf{u}_i \quad (24)$$

where  $NP$  is the number of the supporting nodes of point  $\mathbf{x}$ ,  $\mathbf{u}_i = \{u_i, v_i\}^T$  is the displacement vector at node  $i$ , and  $\bar{\mathbf{B}}_{k(C)}^i$  is the smoothed strain matrix given by

$$\bar{\mathbf{B}}_{k(C)}^i = \begin{bmatrix} \bar{b}_{kx(C)}^i & 0 \\ 0 & \bar{b}_{ky(C)}^i \\ \bar{b}_{ky(C)}^i & \bar{b}_{kx(C)}^i \end{bmatrix} \quad (25)$$

in which

$$\begin{aligned} \bar{b}_{kx(C)}^i &= \frac{1}{A_{k(C)}} \sum_{J=1}^{N_{sgem}} [n_{lx} l_J \sum_{J=1}^{N_C} \varphi_i(\mathbf{x}_{Jl})] \bar{b}_{ky(C)}^i \\ &= \frac{1}{A_{k(C)}} \sum_{J=1}^{N_{sgem}} [n_{ly} l_J \sum_{J=1}^{N_C} \varphi_i(\mathbf{x}_{Jl})] \end{aligned} \quad (26)$$

where  $l_J$  is the length of  $J$ th segment of the smoothing cell,  $N_{sgem}$  the number of the segment of the smoothing cell,  $N_C$  the number of the Gauss points used in each segment,  $n_{lx}$  and  $n_{ly}$  the components of the outward unit normal to the  $J$ th boundary

segment, and  $\mathbf{x}_j$  the coordinate vector of the  $j$ th gauss point on the  $l$ th segment.

One assume that the material parameters  $E, \nu$  are same over a smoothing cell, the smoothed stress in smoothing cell  $\Omega_{k(C)}$  can be easily obtained by

$$\bar{\boldsymbol{\sigma}}_{k(C)} = \mathbf{D}\bar{\boldsymbol{\epsilon}}_{k(C)} \tag{27}$$

### 5. Discretized system equations

#### 5.1. Static analysis

We now seek for a weak form solution of displacements that satisfies the following generalized smoothed Galerkin (GS-Galerkin) weak form that allows the use of discontinuous displacement functions [21]

$$\int_{\Omega} \delta \bar{\boldsymbol{\epsilon}}^T \bar{\boldsymbol{\sigma}} d\Omega - \int_{\Omega} \delta \mathbf{u}^T \mathbf{b} d\Omega - \int_{\Gamma_t} \delta \mathbf{u}^T \mathbf{t}_r d\Gamma = 0 \tag{28}$$

Substituting Eqs. (14), (24) and (27) into Eq. (28), a set of discretized algebraic system equations can be obtained in the following matrix form:

$$\bar{\mathbf{K}}\mathbf{d} - \mathbf{f} = 0 \tag{29}$$

where  $\mathbf{f}$  is the force vector defined as

$$\mathbf{f} = \int_{\Omega} \boldsymbol{\Phi}^T(\mathbf{x})\mathbf{b}d\Omega + \int_{\Gamma_t} \boldsymbol{\Phi}^T(\mathbf{x})\mathbf{t}_r d\Gamma \tag{30}$$

in which  $\boldsymbol{\Phi}^T(\mathbf{x})$  is the shape function vector to build force vector.

In Eq. (29),  $\bar{\mathbf{K}}$  is the (global) smoothed stiffness matrix assembled in the form of

$$\bar{\mathbf{K}}_{ij} = \sum_{k=1}^{N_{\text{cell}}} \bar{\mathbf{K}}_{ij(k)} \tag{31}$$

where the summation means an assembly process same as the practice in the FEM,  $N_{\text{cell}}$  is the number of the background cells of the whole problem domain  $\Omega$ , and  $\bar{\mathbf{K}}_{ij(k)}$  is the stiffness matrix associated with  $\Omega_k$  that is computed using

$$\bar{\mathbf{K}}_{ij(k)} = \sum_{C=1}^{SC} \int_{\Omega_{k(C)}} (\bar{\mathbf{B}}_{k(C)}^i)^T \mathbf{D}(\bar{\mathbf{B}}_{k(C)}^j) d\Omega = \sum_{C=1}^{SC} (\bar{\mathbf{B}}_{k(C)}^i)^T \mathbf{D}(\bar{\mathbf{B}}_{k(C)}^j) A_{k(C)} \tag{32}$$

in which  $SC$  is number of the smoothing cells,  $A_{k(C)}$  and  $\bar{\mathbf{B}}_{k(C)}$  are the area and smoothed curvature-deflection matrix of the  $C$ th smoothing cell, respectively.

#### 5.2. Vibration analysis

The discretized dynamic equilibrium equation is obtained using the GS-Galerkin weak form by simply treating the dynamic inertial force as an “external” force

$$\int_{\Omega} \delta \bar{\boldsymbol{\epsilon}}^T \bar{\boldsymbol{\sigma}} d\Omega = \int_{\Omega} \rho \delta \mathbf{u}^T \ddot{\mathbf{u}} d\Omega \tag{33}$$

where  $\rho$  is the density of the material, and  $\ddot{\mathbf{u}}$  the accelerations can be expressed in terms of the nodal accelerations  $\ddot{\mathbf{u}}_i$  and the shape functions  $\boldsymbol{\phi}_i(\mathbf{x})$

$$\ddot{\mathbf{u}}(\mathbf{x}) = \sum_{i=1}^n \boldsymbol{\phi}_i(\mathbf{x})\ddot{\mathbf{u}}_i \tag{34}$$

Substituting Eqs. (24), (27) and (34) into Eq. (33) yields

$$\bar{\mathbf{K}}\mathbf{u} - \bar{\mathbf{M}}\ddot{\mathbf{u}} = 0 \tag{35}$$

where  $\bar{\mathbf{K}}$  is the smoothed stiffness matrix given in Eq. (31), and  $\bar{\mathbf{M}}$  is the mass matrix given by

$$\bar{\mathbf{M}}_{(k)} = \text{diag}\{\mathbf{m}_1 \ \mathbf{m}_2 \ \mathbf{m}_3\} \tag{36}$$

where  $\bar{\mathbf{M}}_{(k)}$  is sub-matrices of the mass matrix corresponding to cell  $k$ , and  $\mathbf{m}_i$  is the lumped mass at the node  $i$  given by

$$\mathbf{m}_i = \text{diag}\{(\rho A_k/3) \ (\rho A_k/3)\} \tag{37}$$

A general solution to Eq. (35) can be written as

$$\mathbf{u} = \mathbf{Z}_p e^{i\omega_p t} \tag{38}$$

Substituting Eq. (38) into Eq. (35) yields the eigen equation

$$(\bar{\mathbf{K}} - \omega_p^2 \bar{\mathbf{M}})\mathbf{Z}_p = 0 \tag{39}$$

where  $\omega_p$  is the natural frequency associated with the  $p$ th mode and  $\mathbf{Z}_p$  is the corresponding eigenvector.

### 6. Numerical implementation

#### 6.1. Division of smoothing cells and supporting node selection

In the present work, the problem domain is first discretized with background parent cells. Each parent cell is then further divided into  $SC$  smoothing cells. As shown in Fig. 2, triangular background cell with 1, 3 and 4 smoothing cells are considered in this work.

Only shape functions of the integration points on boundary of the smoothing cells need to be evaluated. In constructing the RPIM shape functions, supporting nodes selected using the T2L-scheme introduced by Liu and Zhang [16]. The T2L-scheme selects two layers of nodes to perform interpolation based on triangular cells. As shown in Fig. 3, for the point of interest  $\mathbf{x}_i$  located in a cell, the first layer of nodes refers the three nodes  $i_1, i_2$  and  $i_3$  of the home cell  $i$ , and the second layer contains those nodes which are directly connected to the three nodes of the first layer. For the

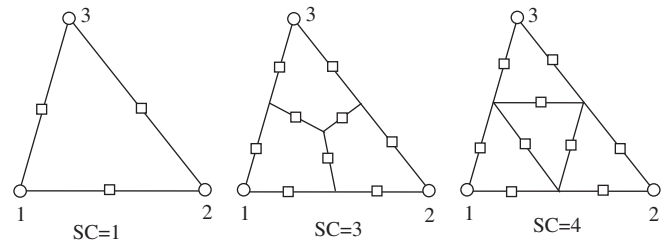


Fig. 2. Division of a parent cell into  $SC$  smoothing cells. The circle presents the field node, the square denotes the integration sampling point.  $SC = 1$  means only one smoothing cell for each background parent cell;  $SC = 3$  means three smoothing cells for each parent cell;  $SC = 4$  means four smoothing cells for each parent cell.

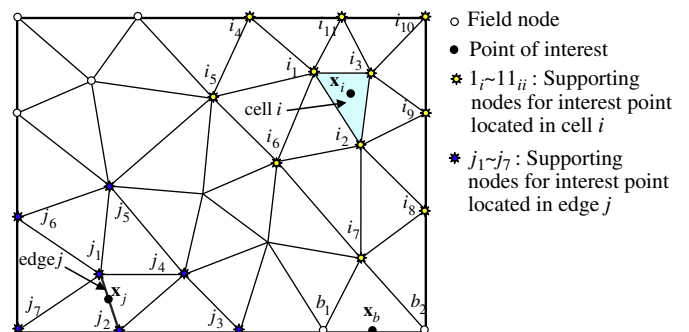


Fig. 3. Supporting node selection for RPIM shape function construction. For interior point  $\mathbf{x}_i$  in a cell  $i$ , the supporting nodes are  $i_1-i_{11}$ . For on-edge point  $\mathbf{x}_j$  on an edge  $j$ , nodes  $j_1-j_7$  are selected as the supporting nodes.

point of interest  $\mathbf{x}_j$  local on an edge  $j$ , the first layer of nodes refers the two nodes  $j_1$  and  $j_2$  of the edge  $j$  and the second layer contains those nodes which are directly connected to the two nodes of the first layer. This scheme can usually select sufficient but not-too-excessive nodes and leads to less time consuming than the traditional schemes used in meshfree methods, in which circular supporting domain is used [10]. We can use this scheme to create RPIM shape functions with high order of consistence for a point of interest and for extremely irregularly distributed nodes.

## 6.2. Conforming and non-conforming models

### 6.2.1. On imposing the essential boundary conditions

Due to the high order nature of the RPIM shape functions, care must be taken in treating lower order essential boundary conditions. For example, in the standard patch tests, linear variation of displacements on the boundary of the problem domain (patch) needs to be imposed. In doing so, we have two schemes: using the RPIM shape functions as per normal, and using linear polynomial interpolation for points on the boundary of the problem domain (patch). These two schemes are denoted as  $SCn$  and  $SCn-L$ , respectively, in which  $n$  denotes the number of smoothing cells. In the numerical examples, we will examine in detail the effects of these two schemes.

### 6.2.2. On conformability

In this work, the RPIM shape functions are created using the MQ-RBF augmented with the linear polynomial basis ( $m = 3$ ), and the shape parameters  $q$  is taken as 1.03,  $\alpha_c$  is taken as 0.35. Some of the reasons for such choices can be found in [22].

It is known that the nodal RPIM shape functions constructed using local nodes are incompatible, meaning that it is discontinuous at locations where the supporting nodes in the support domain are updated [10]. The present CS-RPIM can have two implementations: conforming and non-conforming. In the conforming CS-RPIM, for all the “interior” points on the segments located entirely within a parent cell, the set of RPIM shape functions created are the same, due to the use of the same nodes selected by the T2L-scheme associated with the parent cell. For all the “on-edge” points on the segments that coincide with a cell-edge, the set of RPIM shape functions are created using the nodes selected using the T2L-scheme associated with the cell-edge. Therefore, the RPIM shape functions for these “interior” points are different from those for the “on-edge” points. For each triangular parent cell, we need to create four sets of RPIM shape functions: one set for these “interior” points and three sets for each of the three edges of the parent cell. Of course, these three sets of shape functions for cell edges can be shared by the corresponding neighboring parent cell. When these four sets of RPIM shape functions are used with the  $SCn-L$  scheme, the CS-RPIM model is *conforming*, because the compatibility of the nodal RPIM shape functions on all the smoothing cell edges are ensured in this implementation.

In the non-conforming CS-RPIM, we use the set of “interior” RPIM shape functions of a parent cell also for all the “on-edge” points on the parent cell. In this case only one set of RPIM shape functions is needed for each parent cell, and it will be cheaper. In this case, however, the model becomes non-conforming regardless of  $SCn-L$  or  $SCn-L$  schemes are used, because the nodal RPIM shape functions on the edges of the parent cell are not continuous.

In addition, when the four sets of RPIM shape functions are used but with the  $SCn$  scheme, the CS-RPIM model is still non-conforming due to the improper enforcement of the essential boundary conditions.

The conforming CS-RPIM can, but the non-conforming CS-RPIM cannot pass the standard patch test, as will be shown in the next section. The standard patch test is a straightforward way to examine numerically whether or not a model is conforming or non-conforming.

### 6.3. Patch test

Satisfaction of the standard patch test requires that the displacements of all the interior nodes inside the patch follow “exactly” (to machine precision) the same linear function of imposed displacement on the boundary of the patch. Numerically, passing the standard patch test can ensure a numerical method convergence to the exact solution [23].

Considering a square patch, the regularly and irregularly distributed nodes with the triangular meshes are depicted in Fig. 4. A prescribed linear displacement field is imposed on the boundary  $\Gamma_u$  of the patch are computed using

$$u = 0.001(x + y) \quad v = 0.001(x - y) \quad (40)$$

The material properties of patch are  $E = 1.0$  and  $\nu = 0.25$ . To satisfy the patch test, the linear displacement field approximated exactly, and the numerical solution at any interior nodes should be in exact agreement the analytic ones given in Eq. (40). To examine the numerical error precisely, an error norm in displacement is defined as

$$E_d = \sqrt{\frac{\sum_{I=1}^{N_{\text{node}}} (\mathbf{u}_I^{\text{exact}} - \mathbf{u}_I^{\text{num}})^T (\mathbf{u}_I^{\text{exact}} - \mathbf{u}_I^{\text{num}})}{\sum_{I=1}^{N_{\text{node}}} (\mathbf{u}_I^{\text{exact}})^T (\mathbf{u}_I^{\text{exact}})}} \quad (41)$$

where the superscript *num* denotes the displacement vector obtained using numerical methods, *exact* denotes the exact or analytical solution, and  $N_{\text{node}}$  is the number of total field nodes.

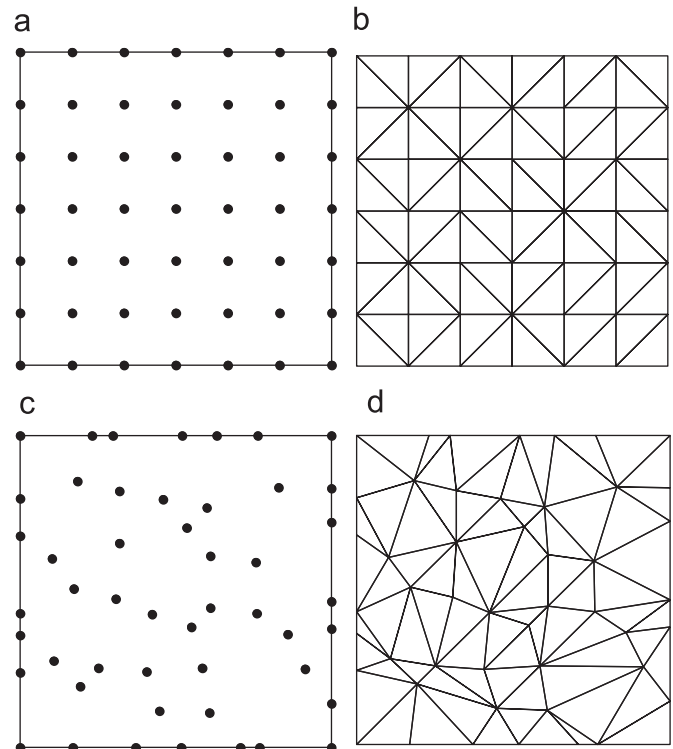


Fig. 4. Node distribution and background cells used for the standard patch test: (a) and (b) regular; (c) and (d) irregular.

**Table 1**  
Displacement error norm of numerical results for the standard patch test using both compatible and incompatible CS-RPIM models.

	Regularly distributed nodes		Irregularly distributed nodes	
SC1-L (CS-RPIM)	6.22970198E-15	Pass	9.84633670E-15	Pass
SC1	1.05153749E-03	Not pass	6.59095620E-03	Not pass
SC3-L	5.44769659E-15	Pass	6.55150660E-15	Pass
SC3	7.48529146E-04	Not pass	3.65510243E-03	Not pass
SC4-L	5.06675634E-15	Pass	8.00943565E-15	Pass
SC4	6.77383258E-04	Not pass	3.54213201E-03	Not pass

Table 1 lists the displacement norm errors of the numerical results for standard displacement patch test using both regularly and irregularly distributed field nodes. It can be found that all the conforming CS-RPIM models (four sets of RPIM shape functions per parent cell with the SCn-L scheme) can pass the patch test to the machine accuracy. All the non-conforming CS-RPIM models (four sets of RPIM shape functions per parent cell with the SCn scheme) cannot pass the patch test and error is of the order of E-03 or E-04.

Note also that although a non-conforming CS-RPIM model cannot pass the patch test, it can produce good (and even better) results for numerical examples which will be shown in next section. Because the non-conforming CS-RPIM models are also cheaper, it may be worthwhile to study them. However, the convergence of such non-conforming models has not yet been proven theoretically, and hence should be used with caution. In this work we study only the non-conforming CS-RPIM models using four sets of RPIM shape functions per parent cell with the SCn scheme.

**7. Numerical examples**

In this section, examples for static and free vibration of solids are presented. It must be point out that the scheme SC1-L in this paper is same as the CS-RPIM proposed in [18], and thus it serves a good comparison. The numerical results obtained from the present method are compared with SC1-L (CS-RPIM) and FEM for showing the effectiveness of the present method.

**7.1. Cantilever beam problem**

A cantilever beam with length  $L$  and height  $D$  is studied as benchmark problem to test the convergence of the method, which is subjected to a parabolic traction at the free end as shown in Fig. 5. The beam is assumed to have a unit thickness so that plane stress condition is valid. The analytical solution from [24] can be given by

$$\begin{aligned}
 u_x(x,y) &= \frac{Py}{6EI} \left[ (6L - 3x)x + (2 + \nu) \left( y^2 - \frac{D^2}{4} \right) \right] u_y(x,y) \\
 &= \frac{-P}{6EI} \left[ 3\nu y^2(L - x) + (4 + 5\nu) \frac{D^2 x}{4} + (3L - x)x^2 \right] \quad (42)
 \end{aligned}$$

where  $I = D^3/12$  is the moment of inertia for the beam.

The stresses corresponding to the displacement equation are

$$\sigma_{xx}(x,y) = \frac{Py}{I}(L - x), \quad \sigma_{yy}(x,y) = 0, \quad \sigma_{xy}(x,y) = \frac{-P}{2I} \left( \frac{D^2}{4} - y^2 \right) \quad (43)$$

The related parameters for the problem are:  $E = 3.0 \times 10^7$  Pa,  $\nu = 0.3$ ,  $L = 48$  m,  $D = 12$  m and  $P = 1000$  N.

Using the same set of triangular meshes, the cantilever beam is studied using the present CS-RPIM method. For comparison, this problem is also studied using FEM triangular element (T3) with the same distributed field nodes. In the numerical computations,

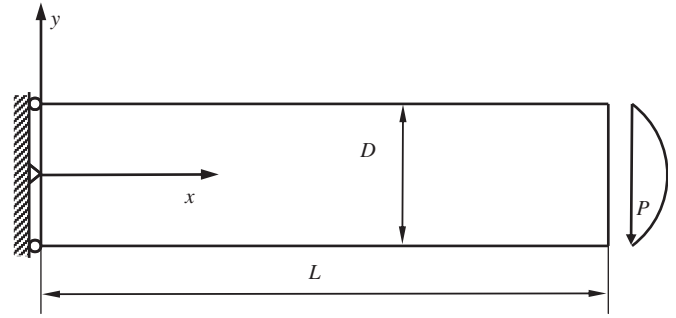


**Fig. 5.** Cantilever beam subjected to a parabolic traction on the right edge of the beam.

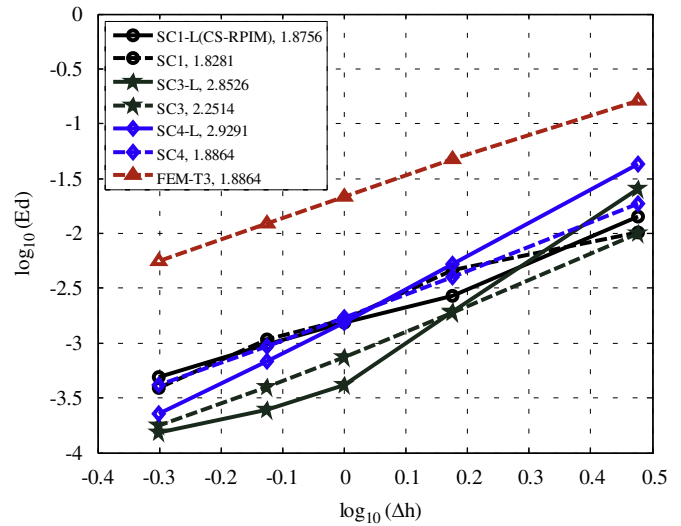


**Fig. 6.** Convergence of the numerical results in displacement error norm for the problem of cantilever beam solved using different methods; the values in the legend are convergence rates.

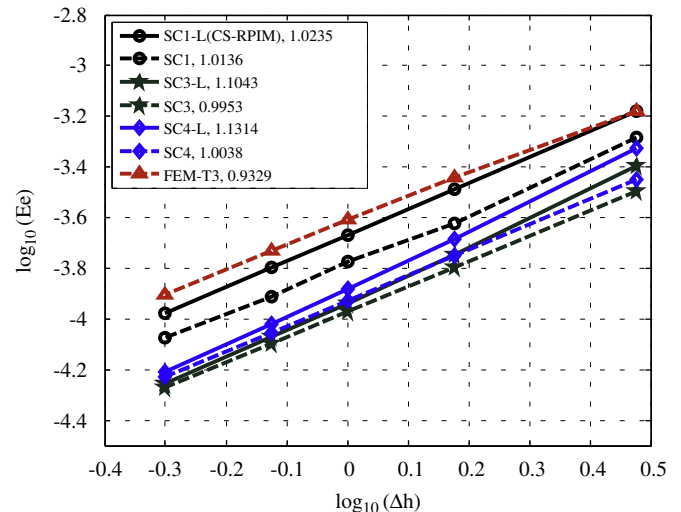


**Fig. 7.** Convergence of the numerical results in energy error norm for the problem of cantilever beam solved using different methods; the values in the legend are convergence rates.

the displacement boundary on the left uses the exact displacements obtained from Eq. (42) and the loading boundary uses the distributed shear stresses in Eq. (43).

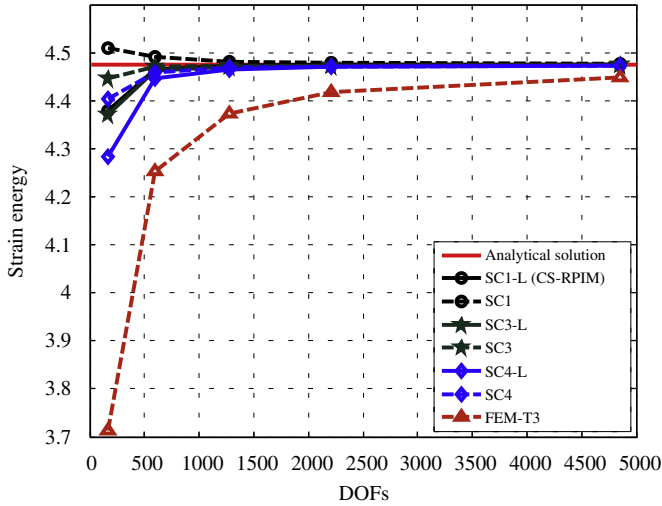


Fig. 8. Solutions (strain energy) converging to the exact solution for the problem of cantilever beam solved using different methods.

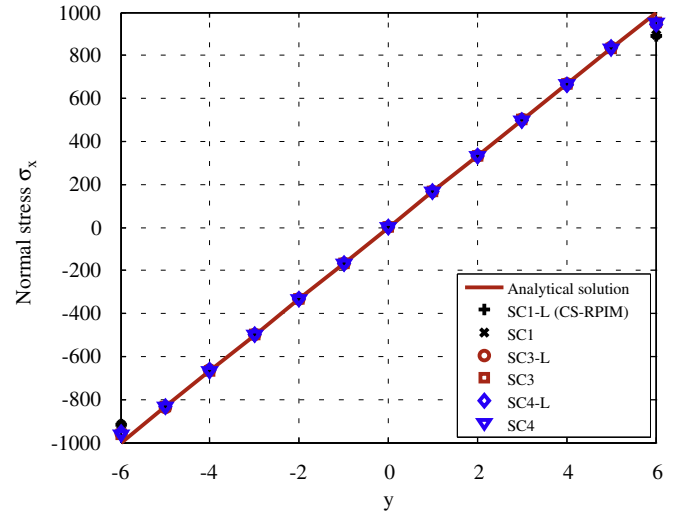


Fig. 10. Normal stress  $\sigma_x$  distribution along the cross-section of the cantilever at  $x = L/2$  obtained using different methods and the same distributed 637 nodes.

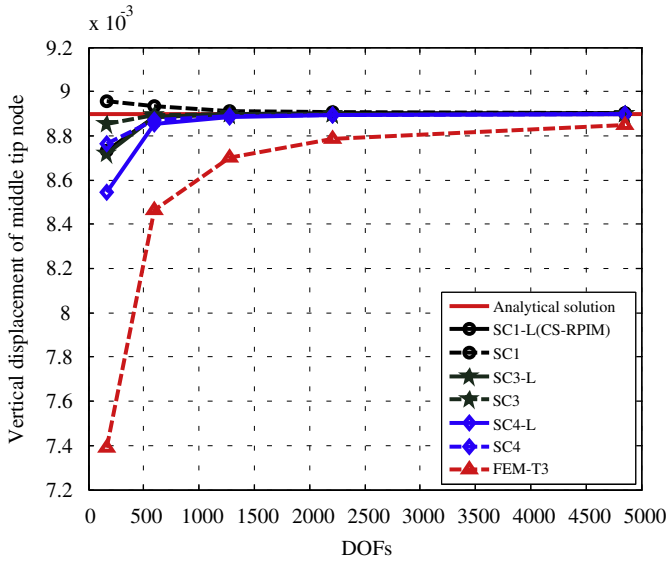


Fig. 9. Solutions (vertical displacement at the node at the middle of the right edge of the beam) converging to the exact solution for the problem of cantilever beam solved using different methods.

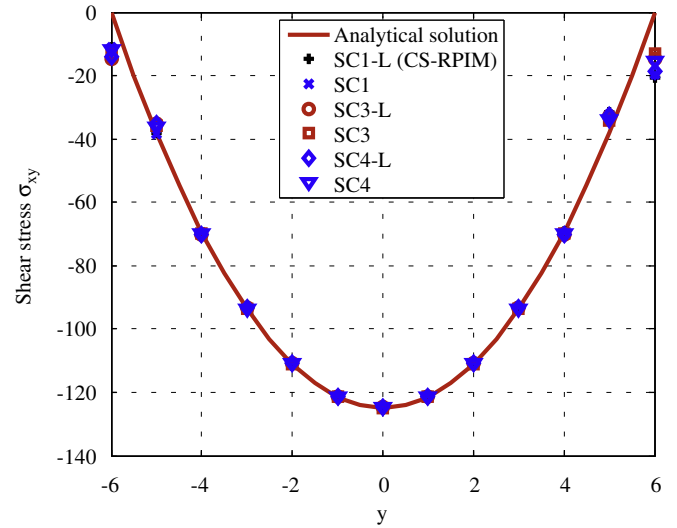


Fig. 11. Shear stress  $\sigma_{xy}$  distribution along the cross-section of the cantilever at  $x = L/2$  obtained using different methods and the same distributed 637 nodes.

Fig. 6 plots the convergence of the solutions in displacement error norm for the cantilever beam solved using different methods. The mesh size parameter  $\Delta h$  is taken to be the average nodal spacing. It can be found that all presented methods are more accurate than FEM (T3). SC3-L gives the best results as compared to the exact ones. SC4-L presents a very high displacement convergence rate, which is much higher even than the theoretical value of 2.0 [23].

Fig. 7 shows the convergence of solutions in energy norm for the cantilever beam solved using different methods. The energy error norm is defined as follows:

$$E_e = \frac{1}{A} \sqrt{\frac{\int_{\Omega} (\boldsymbol{\varepsilon}^{exact} - \boldsymbol{\varepsilon}^{num})^T \mathbf{D} (\boldsymbol{\varepsilon}^{exact} - \boldsymbol{\varepsilon}^{num}) d\Omega}{\int_{\Omega} (\boldsymbol{\varepsilon}^{exact})^T \mathbf{D} (\boldsymbol{\varepsilon}^{exact}) d\Omega}} \quad (44)$$

where  $A$  is the area of the problem domain. It is found that all presented schemes converge faster compared to the FEM (T3). SC4-L gives the highest convergence rate, which is higher than 1.0 that is theoretical value of weak formulation, but lower than

1.5 that is the ideal theoretical value of the  $W^2$  formulation. We find that the accuracy of the energy norm of the non-conforming models (with SC1, SC3 and SC4 schemes) is a little better than corresponding conforming models (with SC1-L (CS-RPIM), SC3-L and SC4-L schemes).

To study the convergence property, the strain energy of the cantilever beam is computed using different methods and plotted in Fig. 8. It is easy to see that SC1 gives upper bound solutions and other methods give lower bound solutions. All the present CS-RPIM models converge very fast to the analytical solution and all provide better accuracy and efficiency than FEM (T3). From these results, one can also find that the numerical model becomes stiff when the number of smoothing cell increases. This finding is in line with those reported in [17] for SFEM models.

The vertical displacements at the node on the middle of the right edge of the cantilever beam computed using different methods are plotted in Fig. 9. The results again show that the presented methods can give much better results than FEM (T3) with the same mesh. The CS-RPIM-SC3 gives the best results compared with other schemes plotted in the figure. Figs. 10 and 11 illustrate the distribution of the normal stress  $\sigma_x$  and shear stress

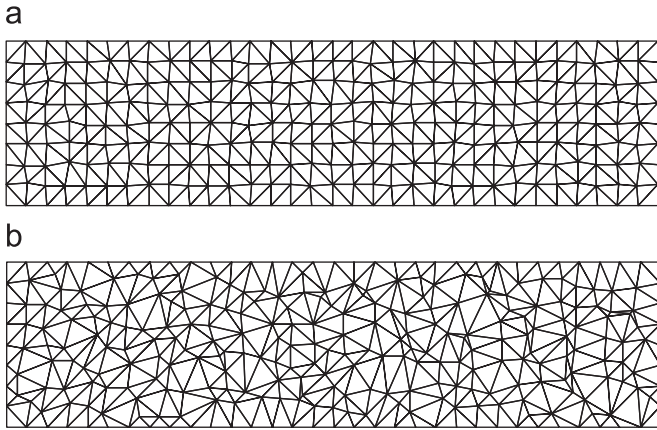


Fig. 12. Irregular meshes with different irregularity factor  $\alpha_{ir}$ : (a)  $\alpha_{ir} = 0.1$ ; (b)  $\alpha_{ir} = 0.5$ .

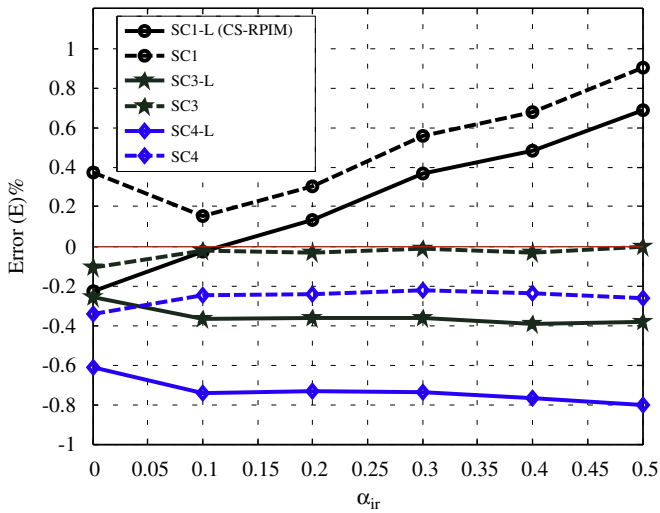


Fig. 13. Relative error of strain energy of the cantilever beam using irregular meshes (mesh  $32 \times 8$ )

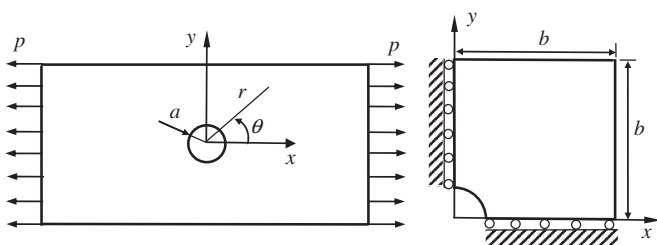


Fig. 14. Infinite plate with a circular hole subjected to uniform tensile and its quadrant model.

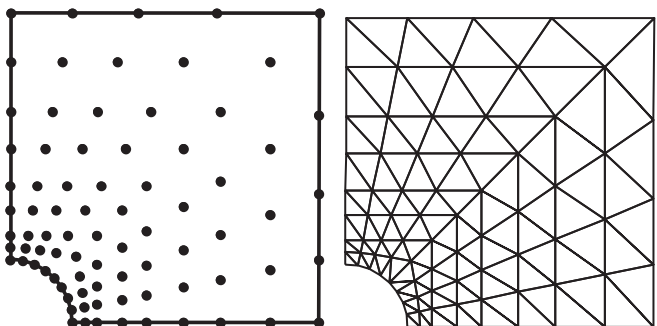


Fig. 15. Domain discretization for the infinite plate with a hole ( $9 \times 9$  nodes).

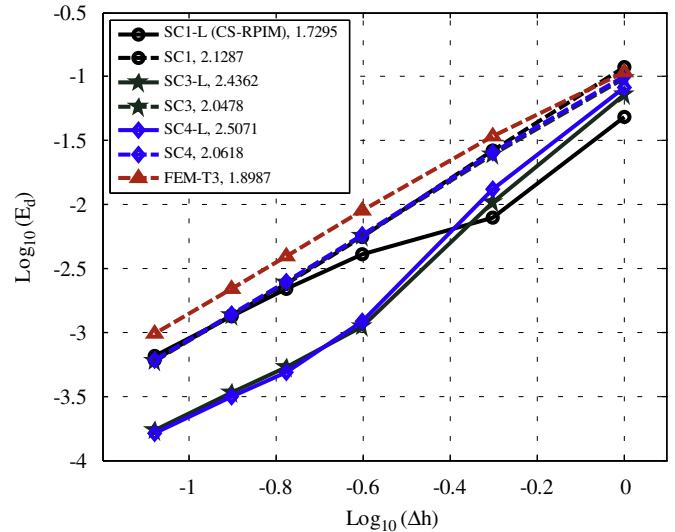


Fig. 16. Convergence of the numerical results in displacement error norm for the problem of infinite plate with a circular hole solved using different methods; the values in the legend are convergence rates.

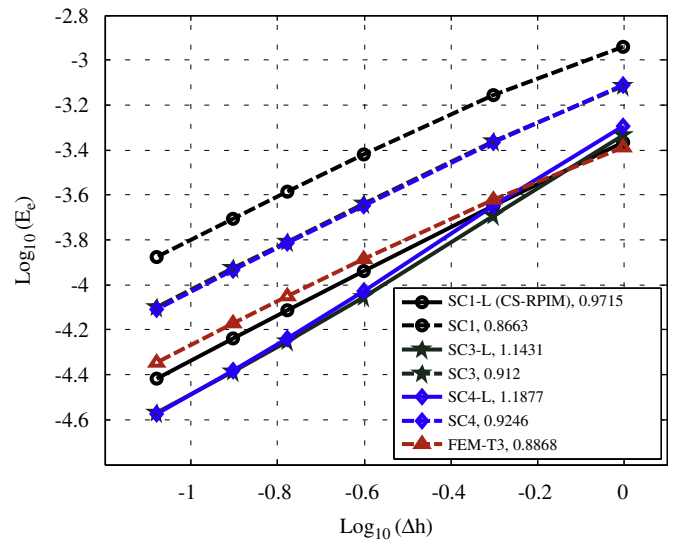


Fig. 17. Convergence of the numerical results in energy error norm for the problem of infinite plate with a circular hole solved using different methods; the values in the legend are convergence rates.

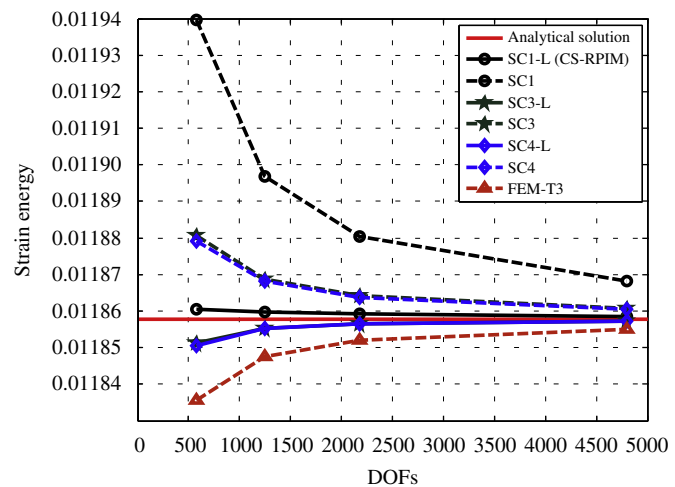


Fig. 18. Solutions (strain energy) converging to the exact solution for the problem of infinite plate with a circular hole solved using different methods.

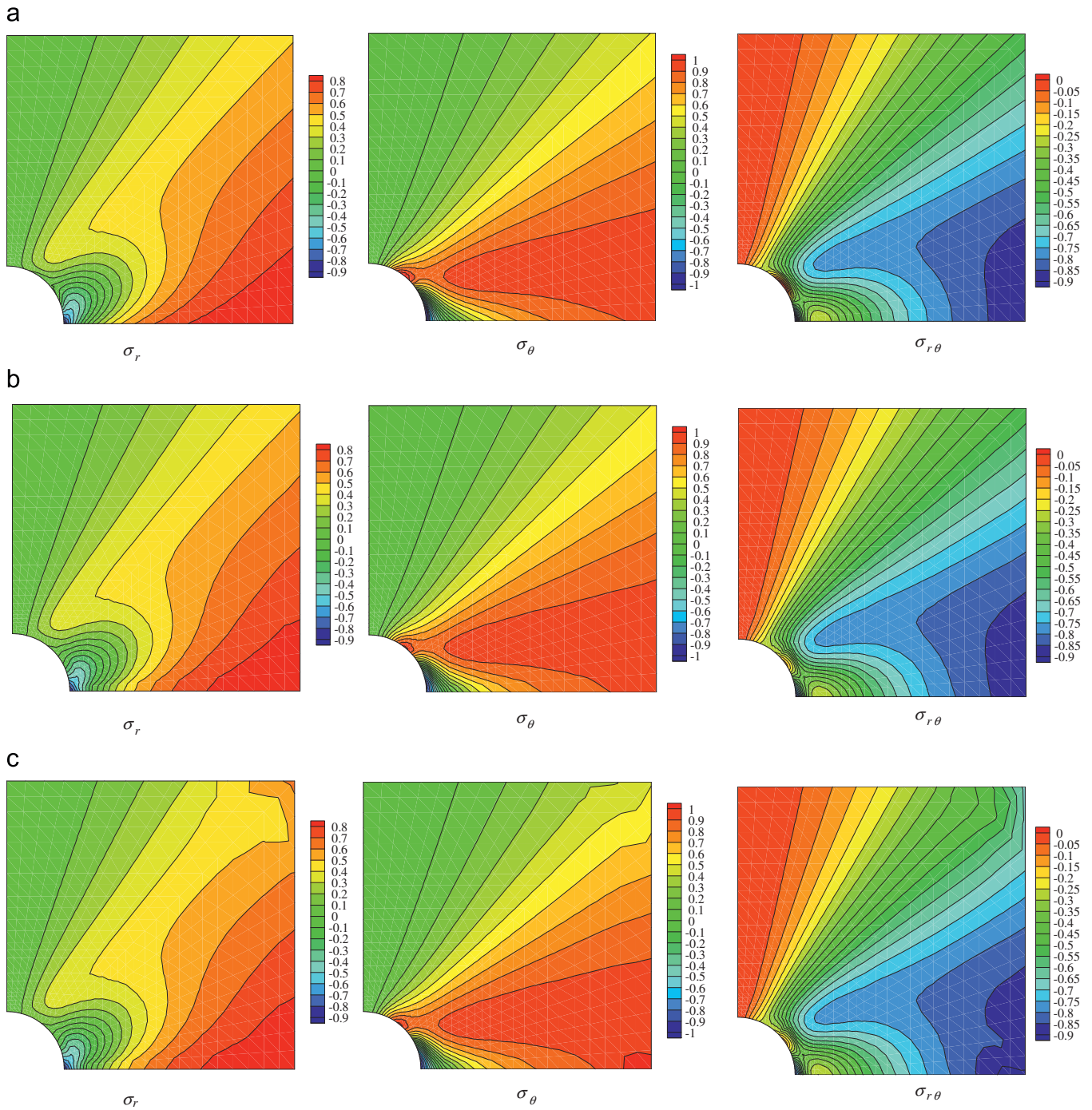


Fig. 19. Stress distributions for the problem of infinite plate with a circular hole: (a) analytical solution; (b) CS-RPIM with SC3-L scheme; (c) CS-RPIM with SC3 scheme.

$\sigma_{xy}$  on the cross-section  $x = L/2$  of the beam. It can be found that the results obtained using present methods agree well with the analytical solutions.

To study the sensitivity of present method to mesh distortion, the cantilever beam is studied using a  $32 \times 8$  mesh. For the distorted mesh, coordinates of the irregular nodes are generated using

$$x_{ir} = x + \Delta x \cdot r_c \cdot \alpha_{ir} \quad y_{ir} = y + \Delta y \cdot r_c \cdot \alpha_{ir} \quad (45)$$

where  $\Delta x$  and  $\Delta y$  are the initial regular nodal spacing in  $x$  and  $y$  direction, respectively,  $r_c$  a computer generated random number between  $-1.0$  and  $1.0$ ,  $\alpha_{ir}$  a prescribed irregularity factor chosen between  $0.0$  and  $0.5$ . Irregular meshes with  $\alpha_{ir} = 0.1$  and  $\alpha_{ir} = 0.5$  are shown in Fig. 12.

Fig. 13 shows the relative errors of strain energy for different methods using irregularly distributed field nodes. It is clearly shown that the present CS-RPIM with SC3, SC3-L, SC4 and SC4-L schemes are insensitive to the mesh distortion even that the meshes are severely distorts with  $\alpha_{ir} = 0.5$ . The relative errors of strain energy for all the schemes are less than 1% even when the severely irregular meshes are used.

### 7.2. Infinite plate with a circular hole

An infinite plate with a circular hole (radius equal to  $a$ ) subjected to a unidirectional tensile load ( $p$ ) in the  $x$  direct is studied. Owing to the symmetry, only one quarter is modeled as

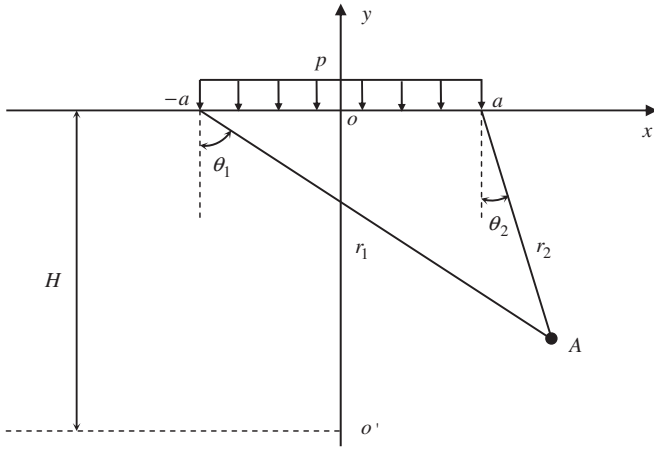


Fig. 20. Semi-infinite plate subjected to a uniform pressure on the upper surface.

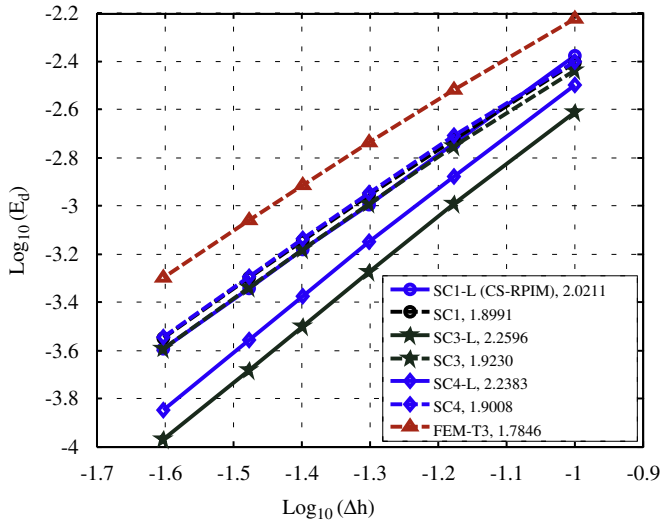


Fig. 21. Convergence of the numerical results in displacement error norm for the problem of semi-infinite plate solved using different methods; the values in the legend are convergence rates.

shown in Fig. 14. Symmetry conditions are imposed on the left and bottom edges, and the inner boundary of the hole is traction free. The analytical solution for the stress can be given in [24]

$$\begin{aligned} \sigma_{xx} &= p \left[ 1 - \frac{a^2}{r^2} \left( \frac{3}{2} \cos 2\theta + \cos 4\theta \right) + \frac{3a^4}{2r^4} \cos 4\theta \right] \sigma_{yy} \\ &= -p \left[ \frac{a^2}{r^2} \left( \frac{1}{2} \cos 2\theta - \cos 4\theta \right) + \frac{3a^4}{2r^4} \cos 4\theta \right] \sigma_{xy} \\ &= -p \left[ \frac{a^2}{r^2} \left( \frac{1}{2} \sin 2\theta - \sin 4\theta \right) - \frac{3a^4}{2r^4} \sin 4\theta \right] \end{aligned} \quad (46)$$

where  $r$  and  $\theta$  are the polar coordinates and  $\theta$  is measured counterclockwise from the positive  $x$ -axis. The displacement fields can be calculated as follows:

$$\begin{aligned} u_r &= \frac{p}{4G} \left\{ r \left( \frac{\kappa + 1}{2} + \cos 2\theta \right) + \frac{a^2}{r} [1 + (\kappa + 1) \cos 2\theta] - \frac{a^4}{r^3} \cos 2\theta \right\} u_\theta \\ &= -\frac{p}{4G} \left[ r - (1 - \kappa) \frac{a^2}{r} + \frac{a^4}{r^3} \right] \sin 2\theta \end{aligned} \quad (47)$$

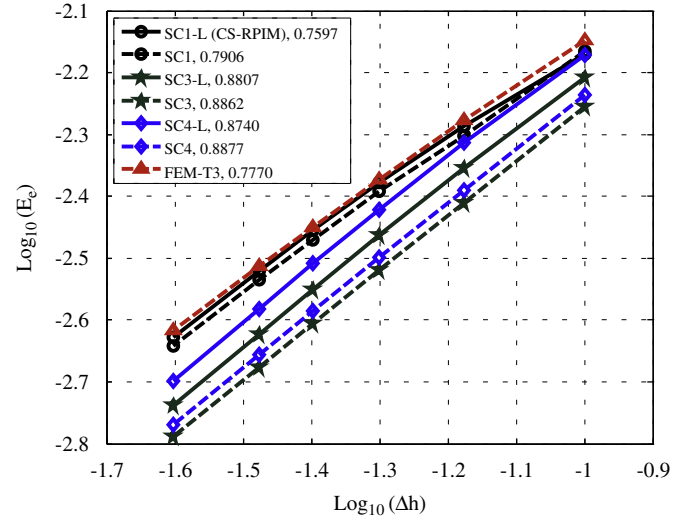


Fig. 22. Convergence of the numerical results in energy error norm for the problem of semi-infinite plate solved using different methods; the values in the legend are convergence rates.

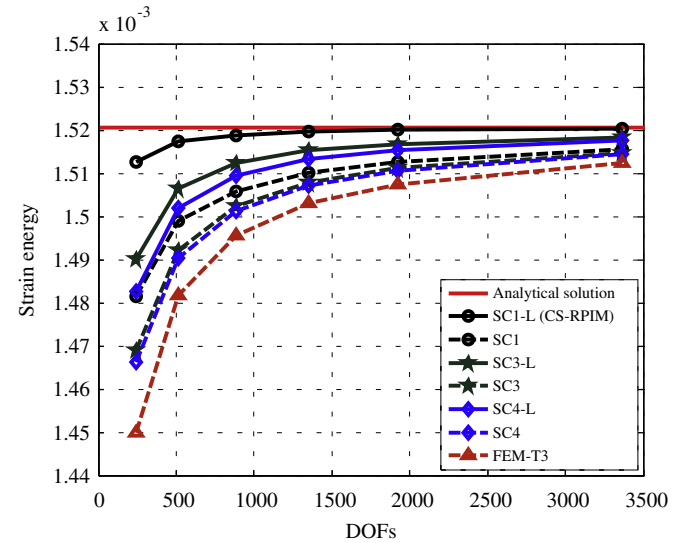


Fig. 23. Solutions (strain energy) converging to the exact solution for the problem of semi-infinite plate solved using different methods.

where

$$G = \frac{E}{2(1 + \nu)}, \kappa = \begin{cases} 3 - 4\nu & \text{for plane stress} \\ \frac{\nu}{1 - \nu} & \text{for plane strain} \end{cases} \quad (48)$$

$E$  is Young's modulus and  $\nu$  is Poisson's ratio.

We studied the problem under plane strain conditions and traction boundary conditions are imposed on the upper and right edges with the analytical stresses obtained using Eq. (46). The parameters for this problem are:  $a = 1$  m,  $b = 5$  m,  $p = 1$  Pa,  $E = 1 \times 10^3$  Pa and  $\nu = 0.3$ . The  $5 \times 5$ ,  $9 \times 9$ ,  $17 \times 17$ ,  $25 \times 25$ ,  $33 \times 33$  and  $49 \times 49$  distributed nodes are used for computation and a  $9 \times 9$  node distribution is shown in Fig. 15.

Fig. 16 plots the convergence of the solutions in displacement error norm for the problem of infinite plate with a circular hole solved using different methods. It can be found that SC3-L and SC4-L exhibit the better accuracy compared with other methods using the same background cells and SC4-L has the highest

**Table 2**  
First six natural frequencies ( $\times 10^4$ ) of a cantilever beam using different CS-RPIM models.

No. of nodes	Mode	SC1-L (CS-RPIM)	SC1	SC3-L	SC3	SC4-L	SC4	Ref. [25]
63	1	0.0887	0.0846	0.0887	0.0830	0.0937	0.0848	0.0926
	2	0.5363	0.5076	0.5322	0.4983	0.5604	0.5094	0.5484
	3	1.2836	1.2825	1.2843	1.2833	1.2846	1.2836	1.2832
	4	1.4251	1.3405	1.4130	1.3192	1.4864	1.3489	1.4201
	5	2.6106	2.4430	2.6014	2.4143	2.7370	2.4702	2.5290
	6	3.8386	3.7318	3.8495	3.7103	3.8535	3.7953	3.7350
306	1	0.0828	0.0824	0.0826	0.0823	0.0831	0.0826	0.0844
	2	0.4960	0.4937	0.4957	0.4935	0.4987	0.4951	0.5051
	3	1.2827	1.2826	1.2828	1.2827	1.2829	1.2827	1.2828
	4	1.3060	1.2987	1.3062	1.2994	1.3141	1.3036	1.3258
	5	2.3728	2.3569	2.3752	2.3608	2.3906	2.3687	2.3993
	6	3.6188	3.5903	3.6256	3.6003	3.6512	3.6129	3.6432

convergence rate (2.5071). For this numerical example, ones can find results of SCn-L are much better than those of SCn, especially for three smoothing cells and four smoothing cells.

Fig. 17 plots the convergence of the solutions in energy error norm for the problem of infinite plate with a circular hole solved using different methods. All methods are found converging well. SC4-L again gives the highest convergence rate (1.1877) in energy norm as in displacement norm, and it is higher than the theoretical value 1.0. It is observed that all of the SCn-L schemes have better accuracy and higher rate of convergence than FEM (T3).

Fig. 18 shows the process of strain energies converging to the analytical one for the infinite plate with a circular hole using different methods. For strain energies, SCn-L schemes have much better accuracy than SCn schemes and FEM. SC3 and SC4 have the same level accuracy as FEM, they all better than SC1. SC1-L (CS-RPIM) converges to the analytical solution as the upper bound solution, whereas SC3-L and SC4-L converge to the analytical one as the lower bound solution. From the results, we still find that the numerical model becomes stiff when the number of smoothing cell increases.

The strain distributions are shown in Fig. 19 for SC3 and SC3-L schemes. It can be found that the results of SC3-L agree well with analytical ones. The results of SC3 are less accurate compared with those of SC3-L and analytical ones, especially in the area near the boundary of the problem. This is because the SC3-L using the linear interpolation on the boundary which leads to the model conforming, and the stress is more smoothing than non-conforming model SC3.

7.3. Semi-infinite plate

A two-dimensional half space subjected to a uniform pressure on the upper surface within a finite range is studied, as shown in Fig. 20. Plane strain condition is considered and the analytical stresses are given by [24]

$$\begin{aligned}
 \sigma_{xx} &= \frac{p}{2\pi} [2(\theta_1 - \theta_2) - \sin 2\theta_1 + \sin 2\theta_2] \sigma_{yy} \\
 &= \frac{p}{2\pi} [2(\theta_1 - \theta_2) + \sin 2\theta_1 - \sin 2\theta_2] \sigma_{xy} \\
 &= \frac{p}{2\pi} [\cos 2\theta_1 - \cos 2\theta_2]
 \end{aligned}
 \tag{49}$$

where  $\theta_1$  and  $\theta_2$  are referred in Fig. 20. The displacement fields can be given as follows:

$$\begin{aligned}
 u_x &= \frac{p(1 - \nu^2)}{\pi E} \left\{ \frac{1 - 2\nu}{1 - \nu} [(x + a)\theta_1 - (x - a)\theta_2] + 2y \ln \frac{r_1}{r_2} \right\} u_y \\
 &= \frac{p(1 - \nu^2)}{\pi E} \left\{ \frac{1 - 2\nu}{1 - \nu} \left[ y(\theta_1 - \theta_2) + 2H \arctan \frac{1}{c} \right] \right. \\
 &\quad \left. + 2(x - a) \ln r_2 - 2(x + a) \ln r_1 + 4a \ln a + 2a \ln(1 + c^2) \right\}
 \end{aligned}
 \tag{50}$$

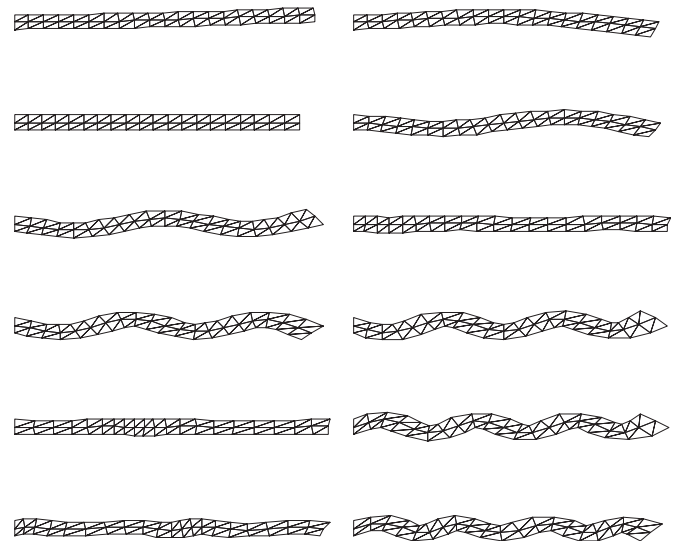


Fig. 24. First 12 modes of the cantilever beam by CS-RPIM with SC3-L.

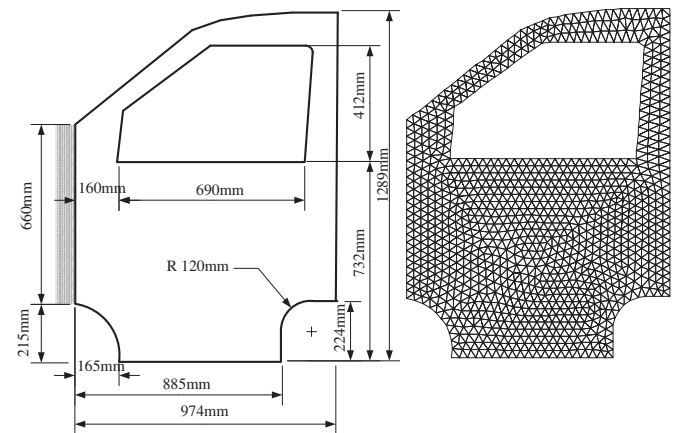


Fig. 25. A simple model of the door of a car

where  $H = ca$  is the distance from the origin to point  $o'$ , where the vertical displacement is assumed to be zero and  $c$  is a coefficient.

Owing to the symmetry about the  $y$ -axis, the problem is modeled with a  $5a \times 5a$  square with  $a = 0.2$  m,  $c = 100$ , and  $p = 1$  KPa. Other parameters are taken as  $E = 3.0 \times 10^7$  Pa and  $\nu = 0.3$ . The left and bottom edges are constrained using exact displacement, while the right side is subjected to tractions computed from the analytical solutions. The problem domain

**Table 3**  
First 12 natural frequencies of the door of a car using different CS-RPIM models.

Mode	CPS3	SC1-L (CS-RPIM)	SC1	SC3-L	SC3	SC4-L	SC4	Reference, CPS6M
1	0.31098	0.29890	0.29934	0.30346	0.30352	0.30498	0.30439	0.30205
2	0.48835	0.45303	0.45299	0.46649	0.46611	0.47208	0.46956	0.46203
3	1.0783	1.0227	1.0191	1.0430	1.0374	1.0522	1.0423	1.0401
4	1.2305	1.2044	1.2044	1.2177	1.2169	1.2217	1.2195	1.2104
5	1.3086	1.2724	1.2706	1.2857	1.2822	1.2911	1.2848	1.2814
6	1.5218	1.4751	1.4733	1.4929	1.4891	1.5003	1.4929	1.4866
7	1.7834	1.6804	1.6785	1.7341	1.7320	1.7537	1.7455	1.7103
8	1.9016	1.8427	1.8408	1.8656	1.8595	1.8747	1.8633	1.8597
9	2.4808	2.3294	2.3203	2.3912	2.3738	2.4177	2.3869	2.3729
10	2.8627	2.7916	2.7880	2.8278	2.8210	2.8412	2.8290	2.8152
11	3.1007	3.0471	3.0456	3.0704	3.0648	3.0785	3.0687	3.0632
12	3.3576	3.2851	3.2784	3.3349	3.3251	3.3466	3.3337	3.3244

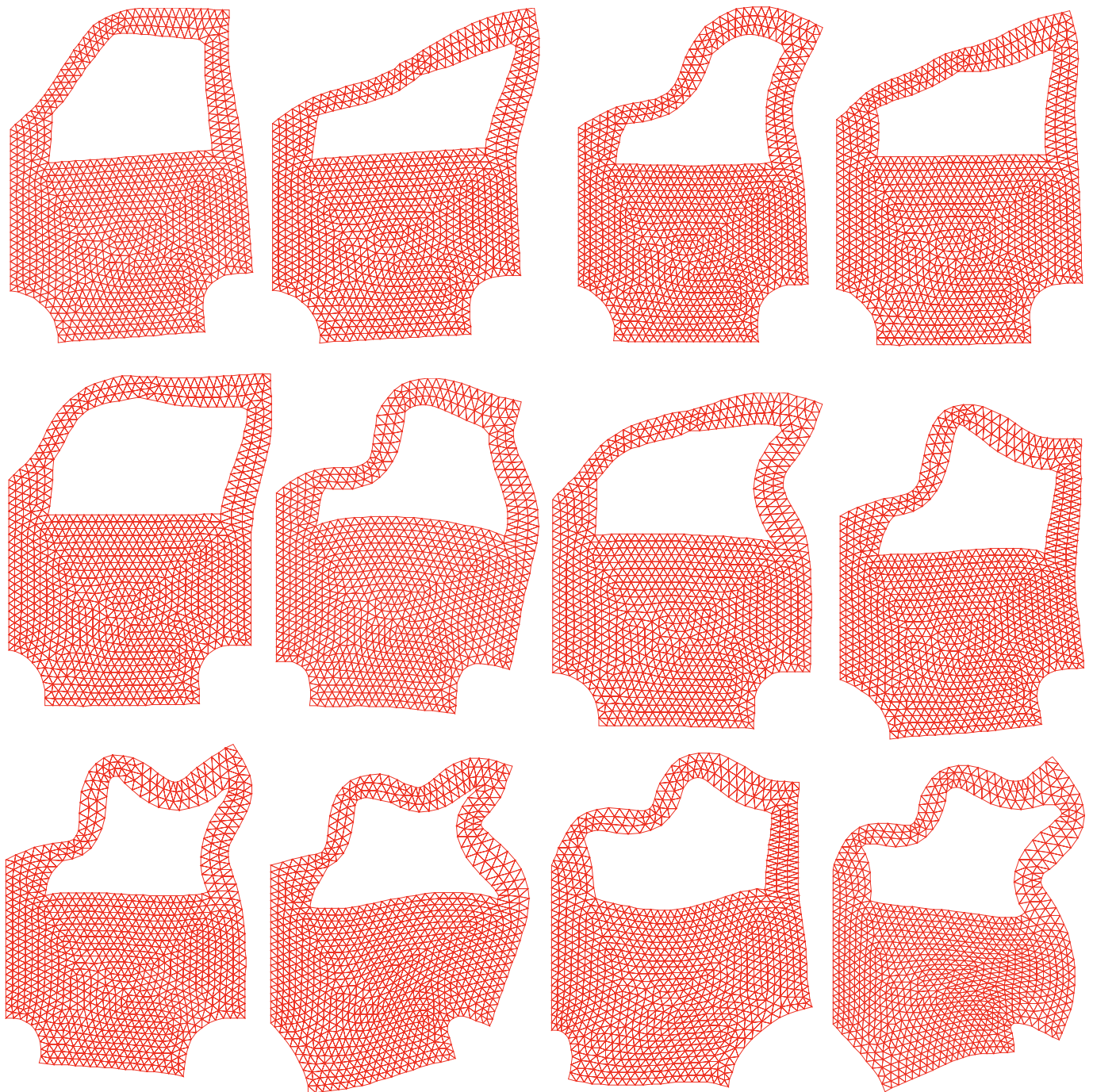


**Fig. 26.** First 12 modes of the door of a car by CS-RPIM with SC3-L.

has been discretized with six models of node distributions (121, 256, 441, 676, 961 and 1681 nodes, respectively) and the convergence rates for the displacement and energy norms are calculated using different methods.

As shown in Fig. 21, all schemes of present method obtain much better accuracy and higher convergence rate for displacement calculation than that of FEM. SC3-L gives the best results and highest convergence rate (2.2596). For this numerical example, ones can find again results of SC $n$ -L are much better than those of SC $n$ , especially for three smoothing cells and four smoothing cells. For convergence in energy error norm shown in Fig. 22, the present methods produce better accuracy and higher convergence rate for energy calculation than the FEM. SC1-L (CS-RPIM) converges lowlier than FEM for coarse mesh, but it converges faster than latter for the fine mesh. The strain energy calculated based on numerical results has been plotted against the number of DOFs in Fig. 23. It can be seen that all schemes possess the better solution than FEM. SC1-L (CS-RPIM) gives the best solution of the strain energy, which is very close to the exact solution even when the meshes are very coarse. Again, we find that results of SC $n$ -L are much better than those of SC $n$  for this problem.

#### 7.4. Free vibration analysis of a cantilever beam

In this example, a cantilever beam is studied with length  $L = 100$  mm, height  $H = 10$  mm, thickness  $t = 1.0$  mm, Young's modulus  $E = 2.1 \times 10^4$  kgf/mm<sup>2</sup>, Poisson's ratio  $\nu = 0.3$ , mass density  $\rho = 8.0 \times 10^{-10}$  kgfs<sup>2</sup>/mm<sup>4</sup>. A plane stress problem is considered. Using the Euler–Bernoulli beam theory we can get its fundamental frequency  $f_1 = 0.08276 \times 10^4$  Hz as a reference. This problem has also been investigated in [25] and the results are used for comparison.

Table 2 lists the first six natural frequencies of the beam, and the first 12 modes using CS-RPIM with SC3-L are demonstrated in Fig. 24. The modes of other present schemes are not shown in the paper as they are very similar to the SC3-L. It is observed that (1) the present method does not have any spurious energy modes; (2) the frequencies agree well with the results obtained in [25]; (3) the frequencies become large with the increase of the smoothing cell, which means the model became stiff with smoothing cell increasing.

#### 7.5. Free vibration analysis of the door of a car

A simple model of the door of a car and the mesh are shown in Fig. 25. The material parameters are given as: Young's modulus  $E = 210$  Mpa, Poisson's ratio  $\nu = 0.3$ , mass density  $\rho = 7.8 \times 10^{-6}$  kg/mm<sup>3</sup>. The thickness of door is  $t = 1.0$  mm. A plane stress problem is considered. The geometry and the mesh are shown in Fig. 25. Numerical results using CPS6M element (6-node triangular element, 3969 nodes) and CPS3 element (3-node triangular element, 1044 nodes) in ABAQUS with the same mesh are computed and used for comparison.

Table 3 lists the first 12 natural frequencies, and the first 12 modes using CS-RPIM with SC3-L are shown in Fig. 26. It is again observed that the frequencies become large with the increase of the smoothing cell for present CS-RPIM. The natural frequencies of SC1 and SC1-L (CS-RPIM) are a little smaller than those of CPS6M, which means the model of CS-RPIM with one smoothing cell is a little softer than CPS6M. When three smoothing cells or four smoothing cells are used, we can find that the results are very closed to the reference solution obtained by CPS6M. The natural frequencies obtained by CPS3 are larger than others as the known overly-stiff phenomenon the linear triangular element.

## 8. Conclusion

In this work, a cell-based smoothing radial point interpolation method (CS-RPIM) is proposed by incorporating the SFEM idea into the standard CS-RPIM method. The background cells are further divided into several smoothing cells and piecewisely constant smoothed strain fields are constructed using the generalized gradient smoothing technique. Only line integrations along the smoothing cells are needed and no derivative of the shape functions is involved in constructing the strain field and to form the stiffness matrix. The support nodes selection for the RPIM approximation uses the T2L-scheme that is based on the background cells and can search the support nodes efficiently. The numerical examples have confirmed the significant features of the present method:

- the conforming CS-RPIM models (four sets of RPIM shape functions per cell with SC $n$ -L scheme) can pass the patch test;
- the non-conforming CS-RPIM models (four sets of RPIM shape functions per cell with SC $n$  scheme) cannot pass the patch test; the essential boundary conditions can be directly imposed as those in finite element method;
- the CS-RPIM needs not evaluate derivatives of meshfree shape functions, and hence is a weakened weak  $W^2$  formulation;
- the CS-RPIM model becomes stiffer when the number of smoothing cell increases;
- the SC3-L scheme always gives more accurate results than other schemes, and hence is recommended;
- all the CS-RPIM models work well with triangular cells, and are very stable and accurate for extremely distributed nodes.

## Acknowledgements

The support of National 973 project (2010CB328005), National Outstanding Youth Foundation (50625519), Key Project of National Science Foundation of China (60635020), Program for Changjiang Scholar and Innovative Research Team in University and the China-funded Postgraduates' Studying Abroad Program for Building Top University are gratefully acknowledged. The authors also give sincerely thanks to the support of Centre for ACES and Singapore-MIT Alliance (SMA), National University of Singapore.

## References

- [1] Monaghan JJ. An Introduction of SPH. *Computer Physics Communications* 1982;48:89–96.
- [2] Nayroles B, Touzot G, Villon P. Generalizing the finite element method: diffuse approximation and diffuse elements. *Computational Mechanics* 1992;10(5): 307–18.
- [3] Belytschko T, Lu YY, Gu L. Element-free Galerkin methods. *International Journal for Numerical Methods in Engineering* 1994;37(2):229–56.
- [4] Liu WK, Jun S, Zhang YF. Reproducing kernel particle methods. *International Journal for Numerical Methods in Engineering* 1995;20:1081–106.
- [5] Onate Idelsohn ES, Zienkiewicz OC, Tylor RL. A finite point method in computational mechanics, applications to convective transport and fluid flow. *International Journal for Numerical Methods in Engineering* 1996;39: 3839–3866.
- [6] Duarte CA, Oden JT. An h-p adaptive methods using clouds. *Computer Methods in Applied Mechanics and Engineering* 1996;139:237–62.
- [7] Atluri SN, Zhu T. A new meshless local Petrov–Galerkin (MLPG) approach in computational mechanics. *Computational Mechanics* 1998;22(2):117–27.
- [8] Liu GR, Gu YT. A point interpolation method for two-dimensional solids. *International Journal for Numerical Methods in Engineering* 2001;50:937–51.
- [9] Wang JG, Liu GR. A point interpolation meshless method based on radial basis functions. *International Journal for Numerical Methods in Engineering* 2002;54:1623–48.
- [10] Liu GR. Meshfree methods: moving beyond the finite element method, 2nd ed.. CRC Press: Boca Raton, USA; 2009.

- [11] Beissel S, Belytschko T. Nodal integration of the element-free Galerkin method. *Computer Methods in Applied Mechanics and Engineering* 1996;139:49–74.
- [12] Bonet J, Kulasegaram S. Correction and stabilization of smooth particle hydrodynamics methods with applications in metal forming simulation. *International Journal for Numerical Methods in Engineering* 1999;47:1189–14.
- [13] Chen JS, Wu CT, Yoon S, You Y. A stabilized conforming nodal integration for Galerkin meshfree methods. *International Journal for Numerical Methods in Engineering* 2001;50:435–66.
- [14] Liu GR. A generalized gradient smoothing technique and smoothed bilinear form for Galerkin formulation of a wide class of computational methods. *International Journal of Computational Methods* 2008;5(2):199–236.
- [15] Zhang GY, Liu GR, Nguyen TT, Song CX, Han X, Zhong ZH, et al. The upper boundary property for solid mechanics of linearly conforming radial point interpolation method (LC-RPIM). *International Journal of Computational Methods* 2007;4(3):521–41.
- [16] Liu GR, Zhang GY. Edge-based smoothed point interpolation methods. *International Journal of Computational Methods* 2008;5(4):621–46.
- [17] Liu GR, Nguyen TT, Dai KY, Lam KY. Theoretical aspects of the smoothed finite element method (SFEM). *International Journal for Numerical Methods in Engineering* 2007;71:902–30.
- [18] Liu GR, Zhang GY. A normed G space and weakened weak (W2) formulation of a cell-based smoothed point interpolation method. *International Journal of Computational Methods* 2009;6:147–79.
- [19] Hardy RL. Theory and applications of the multiquadrics-biharmonic method (20 years of discovery 1968–1988). *Computers and Mathematics with Applications* 1990;19:163–208.
- [20] Golberg MA, Chen CS, Bowman H. Some recent results and proposals for the use of radial basis functions in the BEM. *Engineering Analysis with Boundary Elements* 1999;23:285–96.
- [21] Liu GR. A weakened weak (W2) form for a unified formulation of compatible and incompatible methods, Part I: Theory and Part II: Applications to solid mechanics problems. *International Journal for Numerical Methods in Engineering*, 2009, doi:10.1002/nme.2719.
- [22] Wang JG, Liu GR. On The optimal shape parameters of radial basis functions used for 2-D meshless methods. *Computer Methods in applied Mechanics and Engineering* 2006;191:2611–30.
- [23] Zienkiewicz OC, Taylor RL. *The finite element method*, 5th ed. (V1: The basis). Oxford: Butterworth-Heinemann; 2000.
- [24] Timoshenko SP, Goodier JN. *Theory of elasticity*, 3rd ed.. McGraw-Hill: New York; 1970.
- [25] Nagashima T. Node-by-node meshless approach and its application to structural analysis. *International Journal for Numerical Methods in Engineering* 1999;46:341–85.